Study of $\{11\bar{2}1\}$ Twinning in α-Ti by EBSD and Laue Microdiffraction

LEYUN WANG, ROZALIYA BARABASH, THOMAS BIELER, WENJUN LIU, and PHILIP EISENLOHR

Activity of the $\{11\bar{2}1\}\langle\bar{1}\bar{1}26\rangle$ extension twinning (T2) mode was analyzed in a commercial purity Ti sample after 2 pct tensile strain imposed by four-point bending. The sample had a moderate *c*-axis fiber texture parallel to the tensile axis. Compared with the many $\{10\bar{1}2\}\langle\bar{1}011\rangle$ extension (T1) twins that formed in 6 pct of the grains, T2 twins were identified in 0.25 pct of the grains by scanning electron microscopy (SEM) and electron backscattered diffraction (EBSD) maps. Most of the T2 twins exhibited irregular twin boundaries (TBs) on one side of the twin. High-resolution EBSD revealed both intermediate orientations at some matrix/twin interfaces and substantial lattice rotation within some T2 twins. Interactions between matrix $\langle c + a\rangle$ dislocations $\frac{1}{3}\langle 1\bar{2}13\rangle$ and a $\{11\bar{2}1\}$ T2 twin were investigated by combining SEM/EBSD slip trace characterization and Laue microdiffraction peak streak analysis. $\langle c + a\rangle$ dislocations that originally glided on a pyramidal plane in the matrix were found on other planes in both the matrix and the twin, which was attributed to extensive cross-slip of the screw component, whose Burgers vector was parallel to the twinning plane. On the other hand, thickening of the twin could engulf some pile-up edge components in front of the TB. During this process, these $\langle c + a\rangle$ dislocations transmuted from a pyramidal plane $(0\bar{1}11)$ in the matrix to a prismatic plane $(\bar{1}010)_T$ in the twin lattice. Finally, possible mechanisms for the nucleation and growth of T2 twins will be discussed.

DOI: 10.1007/s11661-013-1714-y

I. INTRODUCTION

MECHANICAL twinning has a large effect on the plasticity of hexagonal metals such as Mg, Ti, and Zr. On one hand, nucleation and propagation of twins in a grain can effectively accommodate deformation along the *c*-axis, thus enhancing the ductility of the material.[1,2] On the other hand, dislocation–twin interaction can make a significant contribution to the work hardening of the material.[3–6] The latent hardening model has typically been used to describe dislocation–twin interaction in crystal plasticity frameworks that generally give good prediction of the measured stress–strain curves.[7,8] However, the latent hardening model may be too simplified to incorporate detailed accommodation mechanisms around twins that were experimentally observed, which include (1) glide dislocations' dissociation at the twin boundary (TB),[4,9,10] (2) transmutation of existing matrix dislocations into the twin lattice,[11–15] (3) formation of kink bands or secondary twins at the twin–twin intersection,[4,10,16,17] etc. Furthermore, cracks can sometimes nucleate at twin–twin or twin-grain boundary intersections because of local shear incompatibility.[18–21] There is not a single computational model that can comprehensively describe twinning in hexagonal metals that include their nucleation, growth, interaction with matrix dislocations, other twins, and grain boundaries. To achieve this aim, more experimental characterization is needed to identify active mechanisms.

Titanium is one of the most widely used hexagonal metals. In Ti, four twinning modes (and their twinning shears, γ) have been reported, namely $\{10\bar{1}2\}\langle\bar{1}011\rangle$ (T1, $\gamma = 0.17$), $\{11\bar{2}1\}\langle\bar{1}\bar{1}26\rangle$ (T2, $\gamma = 0.63$), $\{11\bar{2}2\}\langle 11\bar{2}\bar{3}\rangle$ (C1, $\gamma = 0.10$), and $\{10\bar{1}1\}\langle 10\bar{1}\bar{2}\rangle$ (C2, $\gamma = 0.22$).[22] T1 and T2 are referred to as tensile or extension twinning modes, because generally these two twinning modes result in extension of the crystal in the *c*-direction and can be activated only in such grains that have their *c*-axis strained in tension. Correspondingly, C1 and C2 are referred to as compressive or contraction twinning modes. At room temperature, T1 twinning is the most commonly observed twinning mode in Ti and other hexagonal metals with c/a ratio less than $\sqrt{8/3}$, such as Mg and Zr.[23–29] Several atomistic and grain-scale models have been proposed to account for the nucleation and growth of T1 twins.[30–36] In contrast, other twinning modes have received much less attention.

The current article focuses on the T2 twinning mode. The large shear of T2 twins makes them potential

LEYUN WANG, Postdoc, is with the Nuclear Engineering Division, Argonne National Laboratory, Argonne, IL 60439. Contact e-mail: leyunwang@anl.gov ROZALIYA BARABASH, Staff Scientist, is with the Materials Science and Technology Division, Oak Ridge National Laboratory, Oak Ridge, TN 37831. THOMAS BIELER, Professor, is with the Chemical Engineering and Materials Science, Michigan State University, East Lansing, MI 48824. WENJUN LIU, Physicist, is with the Advanced Photon Source, Argonne National Laboratory, Argonne, IL 60439. PHILIP EISENLOHR, Group Leader, is with the Max-Planck-Institut für Eisenforschung, Max-Planck-Str. 1, 40237 Düsseldorf, Germany.

Manuscript submitted February 3, 2012.
Article published online April 4, 2013

damage nucleation sites in the material. Though T2 twins are less frequent than T1 twins, they have also been observed in Co,[17] Zr,[27,37,38] Ti,[26,29] and an Mg-based alloy.[39] Reed-Hill *et al.* observed kink bands (both inside the twin and outside the twin) adjacent to the tip of some T2 twins in Zr.[37] The kink bands were attributed to a set of basal slip dislocation walls with $\frac{1}{3}\langle 11\bar{2}0\rangle$ Burgers vector. Vaidya and Mahajan[17] examined T2 twins in Co by analyzing dislocations near TBs using transmission electron microscopy (TEM). Near the matrix/twin interface, $\langle c + a\rangle$ dislocations Burgers vector of which was parallel to the twinning plane were identified.[17] Other than these two early articles, little research focusing on T2 twinning has been published, partly because of the lack of effective characterization tools and—at least in the case of Ti—because of the limited number of T2 twin observations compared with T1 twins.

In the last two decades, advances in electron backscattered diffraction (EBSD) and Laue microdiffraction have led to new opportunities for the study of deformation microstructures. Among many applications, EBSD is convenient for statistically analyzing twinning[28,29,38] and characterizing local lattice rotation.[40,41] Laue microdiffraction uses a high-energy polychromatic X-ray microbeam to probe the material. The ultra-brilliant X-ray beam is able to penetrate metals for a distance greater than one hundred microns. Using the differential aperture X-ray microscopy (DAXM) technique,[42–45] Laue diffraction patterns from individual volume elements (voxels) along the beam path can be extracted. Indexing of these Laue patterns reveals the crystal orientation of each voxel with an accuracy as high as 0.01 deg. In a deformed specimen, Laue patterns often display streaked peaks because of the existence of geometrically necessary dislocations (GNDs).[45] By analyzing peak streak direction in a Laue pattern, it is possible to identify the content of local GNDs, which provides new means to gain crucial knowledge about local deformation history.[46,47]

In the current study, T2 twins were identified in five different grains in a commercial purity Ti specimen after small tensile strain. These T2 twins and their parent grains were intensively characterized using EBSD and DAXM. Some unusual features of T2 twins, such as irregular TBs and large orientation gradients inside the twin lattice, were observed. The origin of these features will be discussed.

II. EXPERIMENTAL AND ANALYTICAL METHODS

A. *Sample and Deformation*

The material used in the current study was a rolled and recrystallized grade 1 commercially pure titanium plate with a moderate texture (~6 times random) and an average grain size of 80 μm, per the composition given in Table I. A bend specimen with geometry of 25 mm × 3 mm × 2.5 mm was cut in such a way that the preferred {0001} texture was aligned with its longitudinal axis. Before deformation, the sample surface (25 mm × 3 mm) was polished, finishing with a colloidal silica suspension. Initial EBSD mapping was performed in a region of 5 mm × 3 mm in the center of the surface using a JEOL 6500 SEM equipped with an orientation imaging microscopy (OIM) system (EDAX/TSL, Draper, UT). This region contains 1980 grains according to the automatic grain-counting software in OIM. The specimen was deformed by four-point bending (the bending axis is parallel to the specimen's 3-mm edge) to achieve about 2 pct tensile strain in the central region of the surface, where the stress state was expected to be with uniform tension along the longitudinal direction based on a continuum elastic–plastic FEM analysis.[48] Slip traces and twins on the surface were characterized by the SEM/EBSD combination. Additional details and discussion of the deformation analysis on other specimens from the same material are found in another study.[36]

B. *Laue Microdiffraction and Peak Streak Analysis*

The facilities on beamline 34-ID-E at the Advanced Photon Source (APS) at the Argonne National Laboratory were used for the Laue microdiffraction experiments. The polychromatic synchrotron X-ray beam was focused by a pair of Kirkpatrick-Baez (KB) mirrors onto an X-ray microbeam of about 0.5 μm × 0.5 μm. This microbeam penetrated the sample surface from a 45 deg inclination angle and generated Laue patterns from subsurface regions to a depth of about 200 microns beneath surface along the beam path. A moving Pt wire was used as the differential aperture to block diffracted X-rays in a manner that allowed Laue patterns from individual volume elements along the beam path to be reconstructed.[42–45] With the microbeam scanning on the sample surface, subsurface orientation maps can be built based on the reconstructed Laue patterns.[49]

In the annealed (undeformed) condition, the Laue patterns were characterized by sharp diffraction spots. After deformation, Laue diffraction spots were often streaked, giving evidence of lattice rotations within the diffracting volume, which has been attributed to the presence of GNDs.[45–47] The content of the GNDs dictates the sense of lattice rotation, which in turn determines the peak streak direction.

For a given GND content, the streak direction for any diffraction peak (hkl) can be calculated based on the GND population described using Nye's tensor.[50,51] In Cartesian coordinates, Nye's tensor for a particular type of GND (Burgers vector $\mathbf{b}$, line vector $\boldsymbol{\tau}$, dislocation density ρ) is given by

Table I. Composition (Wt Pct) of Grade 1 Titanium Plate

Element	O	Fe	Al	Cu	C	Ni	S	Cr	N	Ti
Fraction	0.169	0.049	0.017	0.017	0.015	0.013	0.011	0.011	0.004	bal.

$$\alpha_{ij} = \rho b_i \boldsymbol{\tau}_j \quad [1]$$

Nye's tensor can be related to the lattice curvature by[50]:

$$\kappa_{ij} = \alpha_{ji} - \frac{1}{2}\delta_{ij}\alpha_{kk} \quad [2]$$

where κ_{ij} is the curvature tensor describing the magnitude of the rotation around the i-axis for a small position change in the j-direction ($\kappa_{ij} = \frac{d\theta_i}{dx_j}$). The curvature tensor κ_{ij} is related to the lattice rotation tensor ω_{ij} as[51,52]:

$$\omega_{ij} = -\varepsilon_{ijk}\theta_k = -\varepsilon_{ijk}\kappa_{kl}x_l \quad [3]$$

For an edge type of GND, in the "dislocation coordinate system" where the three orthogonal axes x_1, x_2, and x_3 are along the Burgers vector **b**, slip plane normal **n**, and the tangent direction $\boldsymbol{\tau} = \mathbf{b} \times \mathbf{n}$, the only nonzero term in Eq. [1] is $\alpha_{13} = \rho$, so according to Eq. [2], the only nonzero term in the curvature tensor is $\kappa_{31} = \rho$. From Eq. [3], $\omega_{12} = -\omega_{21} = \rho x_1$, and $\omega_{13} = \omega_{31} = \omega_{23} = \omega_{32} = 0$. Before $\boldsymbol{\omega}$ can be used, it must be transformed into a tensor $\boldsymbol{\Omega}$ in the sample coordinate system using the rotation matrix

$$\mathbf{A} = \begin{bmatrix} b_X & b_Y & b_Z \\ n_X & n_Y & n_Z \\ \tau_X & \tau_Y & \tau_Z \end{bmatrix} \quad [4]$$

Here, b_X, b_Y, and b_Z are the three components of **b** along the X, Y, and Z directions, respectively, in the sample coordinate system. n_X, n_Y, n_Z, τ_X, τ_Y, and τ_Z are defined in the same manner for **n** and $\boldsymbol{\tau}$. Finally, the streak direction at any peak (hkl) is given by:

$$\boldsymbol{\xi} = \boldsymbol{\Omega} \cdot \mathbf{g_{hkl}} = \mathbf{A}^T \omega \mathbf{A} \cdot \mathbf{g_{hkl}} \quad [5]$$

It can be verified that Eq. (5) is equivalent to the previously proposed equation $\boldsymbol{\xi} = \frac{\boldsymbol{\tau} \times \mathbf{g_{hkl}}}{|\boldsymbol{\tau} \times \mathbf{g_{hkl}}|}$ that was derived using a more sophisticated diffraction theory.[46,47] For any slip system, possible streak directions at peak (hkl) due to edge GNDs on that slip system can be calculated using Eq. [5] and compared with the experimentally collected diffraction patterns. This method has been successfully used to identify the GND content in a few materials.[47,49,53–55] In the current study, we will use the same method to analyze those diffraction patterns that display straight streaked peaks. However, only edge GNDs can be considered in the analysis.

III. RESULTS

A. *Identification of T2 Twins and Surface Characterization*

In the 5 mm × 3 mm central region on the surface that contains 1980 grains, 116 grains display T1 twins.

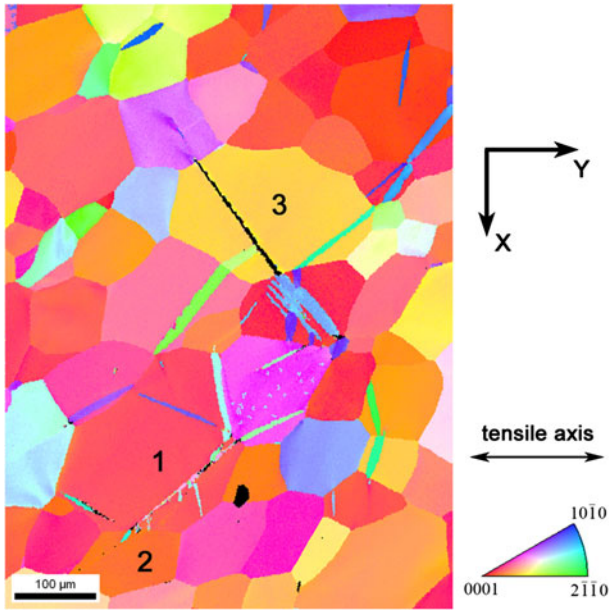

Fig. 1—Inverse pole figure map of an area containing both T1 and T2 twins. In Grains 1, 2, and 3, T2 twins were identified. T2 twins are thinner than most T1 twins. The coordinate system to the right of the map is the basis for Bunge Euler angles and all other maps in the article.

In this same region, T2 twins were only observed in 5 grains in two distinct microstructural areas, which are close to the longitudinal central axis on the surface and about 3.5 mm apart from each other. Figure 1 shows a low magnification inverse pole figure map, in which Grains 1-3 display T2 twins. (The horizontal tensile axis inverse pole figure (IPF) color key is used in all IPF maps in the current study.) These T2 twins are shown in greater detail in Figures 2 and 3 where they are marked by yellow arrows.

In Grain 1, two different T2 twin variants were identified (Figure 2(a)). One variant, ($\bar{1}2\bar{1}1$)[$1\bar{2}16$], was successfully indexed in high-resolution EBSD scans (step size = 0.15 μm) in a pink color in Figures 2(b) and (c). The misorientation between the twin and the parent grain was approximately 35 deg about the [10$\bar{1}$0] axis, consistent with the theoretical misorientation relationship for T2 twinning in Ti.[22] Along its TBs, small regions of dark pink color (an orientation different than the twin and the matrix) were occasionally observed (Figure 2(c)). As shown in an enlarged EBSD map (Figure 2(d)) and the corresponding {0001} and {10$\bar{1}$0} pole figures (Figure 2(e)), the dark pink orientation ((φ_1, Φ, φ_2) = (213 deg, 77 deg, 233 deg)) lies between the twin ((φ_1, Φ, φ_2) = (229 deg, 79 deg, 231 deg)), and matrix orientations ((φ_1, Φ, φ_2) = (14 deg, 103 deg, 61 deg)). The matrix, the twin, and the dark pink orientation have a common [10$\bar{1}$0] crystal direction: their (10$\bar{1}$0) poles (the middle one) coincide in the {10$\bar{1}$0} pole figure, while their ($1\bar{1}$00) and (01$\bar{1}$0) poles are distinct. Misorientation between the twin (or matrix) and the dark pink region is less than 20 deg. Since all the four twinning modes in Ti require a twin/matrix misorientation of at least

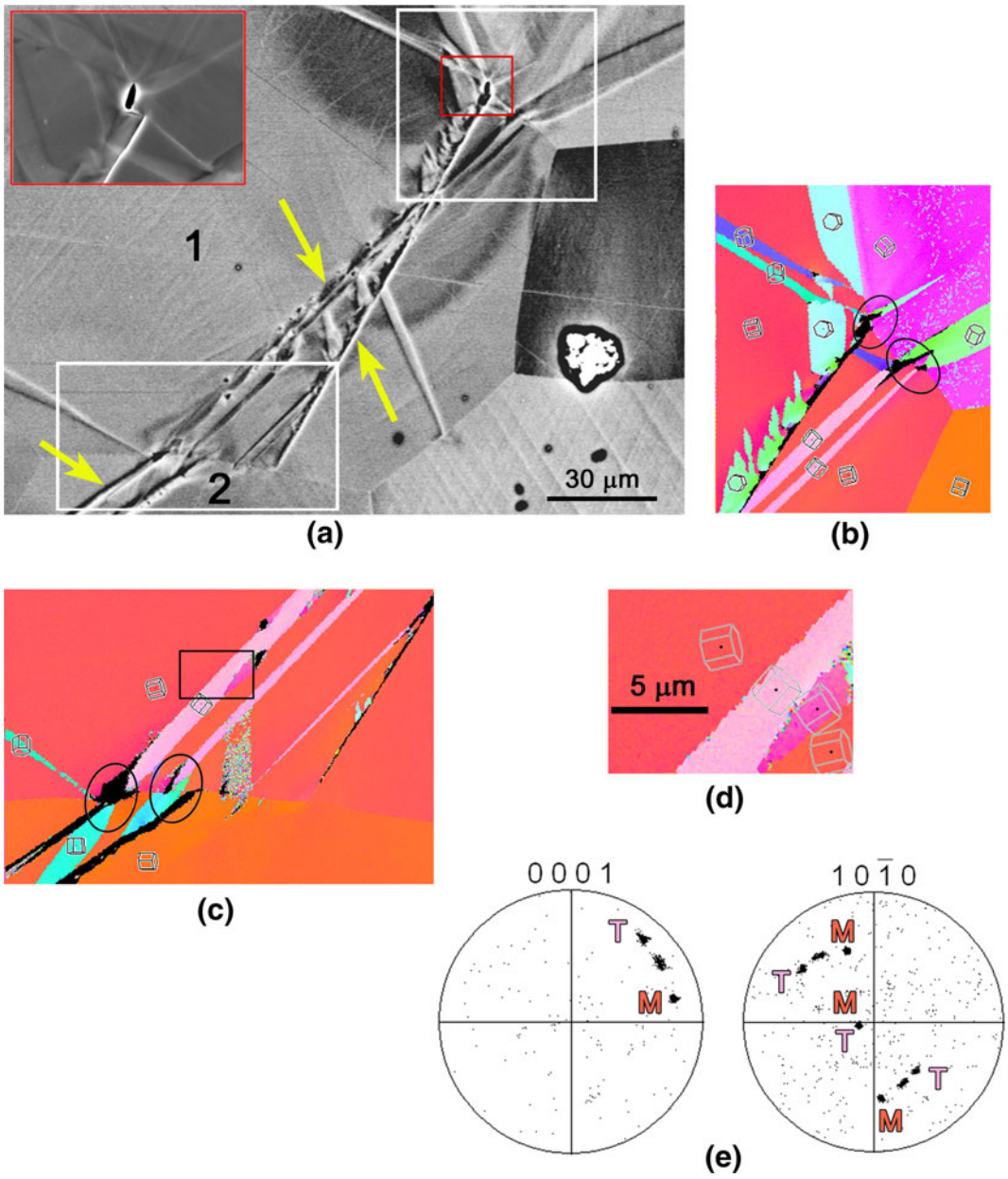

Fig. 2—(*a*) Yellow arrows identify T2 twins in Grains 1 and 2. At the upper end of one T2 twin variant in Grain 1, a microcrack formed. An enlarged image of this microcrack (the area within the red box) is shown in the upper left corner. (*b*) An EBSD map corresponding to the upper-right white box in (a). (*c*) An EBSD maps corresponding to the lower-left white box in (a). (*d*) Small regions with an intermediate orientation (dark pink color) were found on the twin boundary of a T2 twin, as shown in the enlarged EBSD map corresponding to the black box in (c). (*e*) {0001} and {$10\bar{1}0$} pole figures show that the orientation of the dark pink region is almost halfway between the twin orientation ("T") and the matrix orientation ("M").

35 deg,[22] it is unlikely that the dark pink region corresponds to any secondary twinning. Instead, it was more likely a form of kink that accompanied the twin growth, which will be discussed later. The other identified T2 variant in Grain 1 was $(11\bar{2}1)[\bar{1}\bar{1}26]$, which appears black in Figures 2(b) and (c), as the pixels have a low EBSD confidence index owing to their abrupt surface topography. Trace analysis and the surface topography confirm the operation of this twinning system. The T2 variant in Grain 2 was also identified by trace and topographic analysis.

At the intersection of a T2 twin and a grain boundary, a T1 twin is often observed on the other side of the grain boundary (will be referred to as "T2 + T1 twin pair" following[56]). For example, the pink T2 twin in Grain 1 stimulated T1 twins in the adjacent grains from both its upper end and its lower end (see circles in the EBSD maps in Figures 2(b) and (c)). The black T2 twin in Grain 1 also stimulated a T1 twin from its upper end. In addition, a microcrack was observed by a high magnification secondary electron image (inset red box in Figure 2(a)). This microcrack seems to result from the

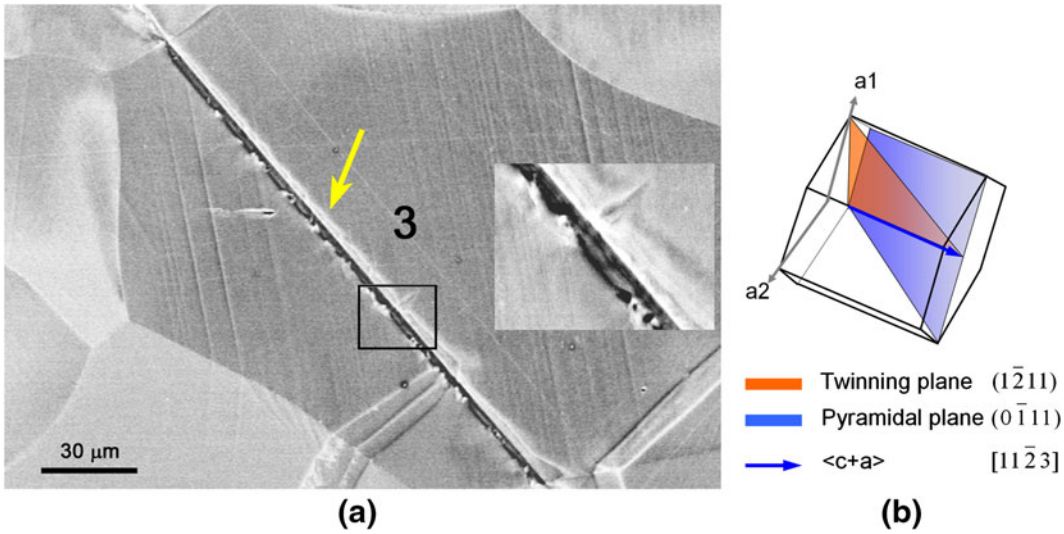

Fig. 3—(*a*) Both T2 twins (yellow arrow) and T1 twins are identified in Grain 3. Part of the T2 twin (the black box) is shown at higher magnification. Grain 3 also has evident slip traces. (*b*) The unit cell of grain 3 ((φ_1, Φ, φ_2) = (157 deg, 78 deg, 28 deg)). The activated pyramidal $\langle c + a \rangle$ slip system $(0\bar{1}11)[11\bar{2}3]$ has its Burgers vector parallel to the operating T2 twinning plane, $(1\bar{2}11)$.

intersection between the unindexed T2 twin coming from lower part and small T1 twins near its upper end. Owing to the misorientation constraint, a T1 twin that impinged on a T2 twin generally cannot cross it by forming a secondary twin as in BCC metals.[10] It is expected that some emissary dislocations may be generated at the intersection of a T1 twin and a T2 twin, which may lead to crack nucleation in a manner that is similar to the model proposed by Sleeskwyk[18] for twin intersections in BCC metals.

Figure 3(a) shows the T2 twin in Grain 3 ((φ_1, Φ, φ_2) = (157 deg, 78 deg, 28 deg)). This twin (twinning system $(1\bar{2}11)[1\bar{2}16]$) has a rough surface topography, and it blocked the growth of two T1 twins from the left. Given its tapered upper end, this T2 twin must have nucleated from its lower end, where many T1 twins nucleated and developed in the grain below (more evident in Figure 1), which is another T2 + T1 example. In addition to twins, distinct slip traces were also observed in Grain 3. By trace and Schmid factor analysis, these slip traces were from the activation of $(0\bar{1}11)[11\bar{2}3]$, a pyramidal $\langle c + a \rangle$ slip system (with a global Schmid factor = 0.494, which is more likely than the other $\langle c + a \rangle$ slip system $(0\bar{1}11)[\bar{1}2\bar{1}3]$ on the same plane with a global Schmid factor of 0.394). $(0\bar{1}11)[11\bar{2}3]$ has a Burgers vector, $\frac{1}{3}[11\bar{2}3]$ that is parallel to the operating T2 twinning plane $(1\bar{2}11)$, as shown in Figure 3(b).

Two other grains display T2 twins shown in Figure 4(a) with yellow arrows. The activated twinning system in Grain 4 ((φ_1, Φ, φ_2) = (175 deg, 66 deg, 2 deg)) was $(\bar{1}\bar{1}21)[11\bar{2}6]$. This twin appears to have stimulated two smaller T2 twins in Grain 5 and massive T1 twins in the grain above (see the inset EBSD map in Figure 4(a)). Its left TB is irregular, while the right TB is straight, but a surface ledge developed along the right TB, which gave rise to the very bright local contrast in Figure 4(a). This twin separated Grain 4 into two parts, with the left part having much stronger slip traces (indicated by a blue line) than the right part. According to trace and Schmid factor analysis, two coplanar pyramidal $\langle c + a \rangle$ slip systems could be activated: $(0\bar{1}11)[\bar{1}2\bar{1}3]$(Schmid factor = 0.447) or $(0\bar{1}11)[11\bar{2}3]$ (Schmid factor = 0.477). Laue microdiffraction and peak streak analysis described later suggest that $(0\bar{1}11)[\bar{1}2\bar{1}3]$ was probably the activated slip system in Grain 4. The topographic features in this area are better shown in Figure 4(b), an image taken from a tilted perspective. The region within the small white box was imaged at higher magnification under both secondary electron (SE) mode and backscattered electron (BSE) mode (Figure 4(c)). From these two images, the height of the ledge is about 1 μm. Slip traces of $(0\bar{1}11)[\bar{1}2\bar{1}3]$ $\langle c + a \rangle$ slip were found on the edge of the ledge as well as on the adjacent surface. Inside the twin, two slip trace directions are evident from the BSE image. They converge at the twin interface in several locations as pairs, suggesting co-nucleation of these slip traces. By trace analysis, they correspond to slip on two pyramidal planes, $(0\bar{1}11)_T$ and $(\bar{1}10\bar{1})_T$ with a common direction $[\bar{1}2\bar{1}3]_T$ (subscript T" means that the crystal plane/direction is defined in the twin lattice). It is known that a matrix dislocation can transmit into the twin lattice without leaving a step on the interface if its Burgers vector is parallel to the twinning plane.[22] Since the activated matrix slip system $(0\bar{1}11)[\bar{1}2\bar{1}3]$ has its Burgers vector parallel to the twinning plane $(1\bar{2}11)$ as well as pyramidal planes $(0\bar{1}11)_T$ and $(\bar{1}10\bar{1})_T$, it is possible that the observed slip traces in the twin were the result of slip transmission. Figure 4(d) shows the geometrical relationship of slip systems $(0\bar{1}11)[\bar{1}2\bar{1}3]$, $(0\bar{1}11)_T[\bar{1}2\bar{1}3]_T$, and $(\bar{1}10\bar{1})_T[\bar{1}2\bar{1}3]_T$ with respect to the TB. From the sense of shear, the cooperative activation of $(0\bar{1}11)_T[\bar{1}2\bar{1}3]_T$ and $(\bar{1}10\bar{1})_T[\bar{1}2\bar{1}3]_T$ would sink the material between each pair of slip traces and elevate the adjacent material. This topographic feature has been

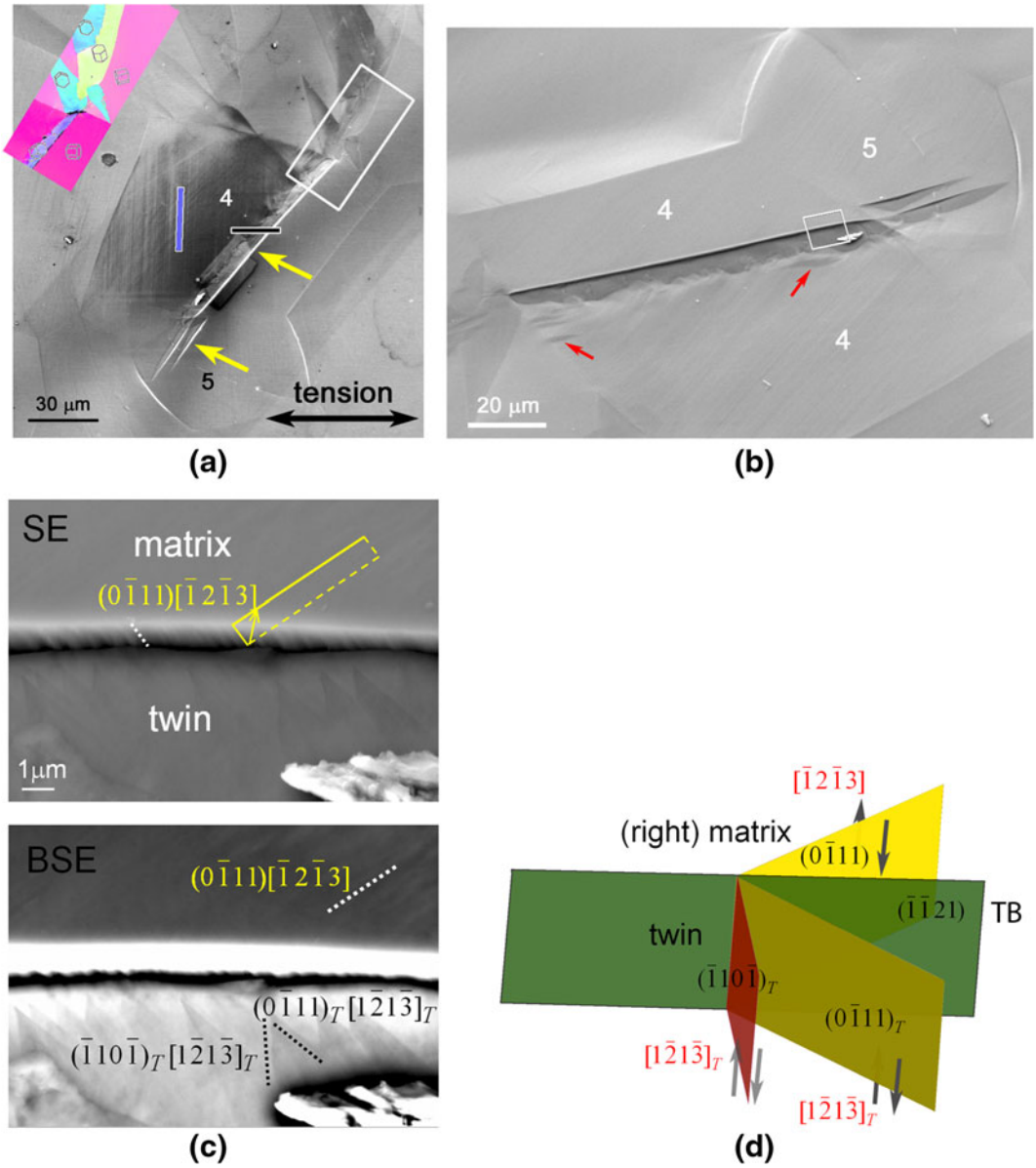

Fig. 4—(*a*) T2 twins observed in Grains 4 and 5 are indicated by yellow arrows. The EBSD map on the upper-left corner corresponds to the white box. In Grain 4, slip traces can be observed to the left of the T2 twin (blue line). The horizontal black line crossing the middle of the twin indicates the location of the Laue microdiffraction line scan shown in Fig. 6. (*b*) An image taken from a rotated and tilted perspective. Some small T1 twins in Grain 4 are marked by red arrows. (*c*) Secondary electron (SE) image and backscattered electron (BSE) image for the region within the white box in (b). $(0\bar{1}11)[\bar{1}2\bar{1}3]$ slip traces can be observed both on the ledge and on the surface. Slip traces in the twin are identified to be $(0\bar{1}11)_T[1\bar{2}1\bar{3}]_T$ and $(\bar{1}10\bar{1})_T[1\bar{2}1\bar{3}]_T$. A mode II microcrack is evident at the base of the ledge. (*d*) Geometrical relationship of the activated slip systems: $(0\bar{1}11)[\bar{1}2\bar{1}3]$, $(0\bar{1}11)_T[1\bar{2}1\bar{3}]_T$ and $(\bar{1}10\bar{1})_T[1\bar{2}1\bar{3}]_T$. They have a common Burgers vector that is parallel to the twinning plane.

confirmed in another tilted SEM image, and it is consistent with the darker BSE contrast in the wedge-like regions bounded by paired slip traces in Figure 4(c).

To further characterize the T2 twin in Grain 4, an EBSD scan with step size of 0.02 μm was performed with the trace of the TB aligned close to the beam direction. Such a setup improved the fraction of high confidence pixel indexing within the twin. This scan covered the twin and the matrix, and it left some visible beam contamination that darkened the surface (see Figure 4(a)) that is related to the surface topography in the twin; note that the scanned area consists of two narrow rectangular areas, with a shaded parallelogram on the twin between them. From the IPF map in Figure 5(a), large orientation gradients are evident in the twin. The orientation spread within the twin is up to 15 deg and appears quite heterogeneous (Figure 5(b)). Figure 5(c) shows the stereographic projection of $\{10\bar{1}0\}$ poles of selected points A–E. A–D were from different places in the twin, while E was from the matrix. The $(1\bar{1}00)$ pole of these five points are relatively close, while their $(10\bar{1}0)$ and $(01\bar{1}0)$ poles are separated. This

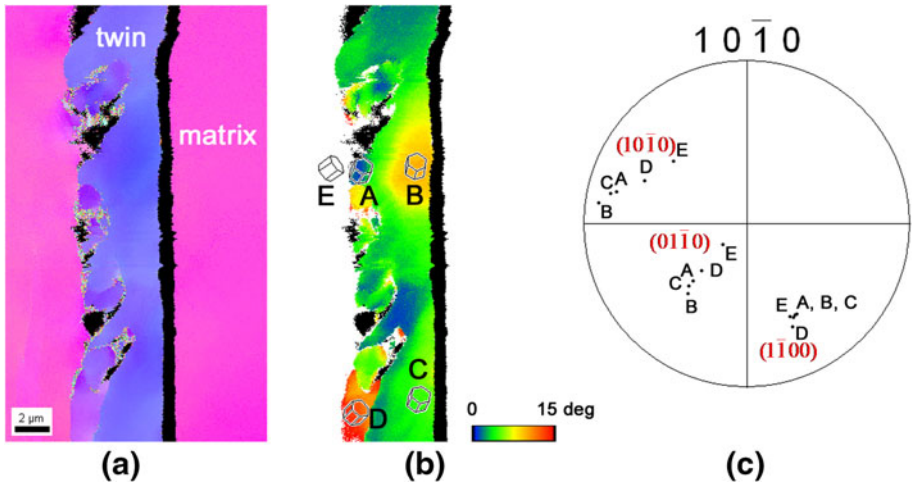

Fig. 5—(*a*) High-resolution EBSD scan shows large orientation gradients within the twin, while the matrix maintained a more near-uniform orientation. (*b*) A map of orientation spread within the twin. Orientations at five points (A–E) are represented by hexagonal unit cells. (*c*) Stereographic projection of orientations A–E showing similarly oriented $(1\bar{1}00)$ poles but divergent $(10\bar{1}0)$ and $(01\bar{1}0)$ poles. The misorientation between E and A was about 35 deg around the $(1\bar{1}00)$ pole.

indicates that the lattice rotation inside the twin was generally around the $[1\bar{1}00]$ axis, same as the twin/matrix misorientation axis.

B. *Laue Microdiffraction Characterization*

A Laue microdiffraction line scan (length = 20 μm, step size = 1 μm) was performed across the middle of the T2 twin in Grain 4. The position of this line scan is indicated in Figure 4(a). Figure 6 shows the resultant subsurface structure of this twin. In this figure, pixels with different colors have different crystal orientations. Three orientations are identified from this scan—Grain 4 (pink), the embedded T2 twin (light purple), and a subsurface grain (light green). Some pixels were unindexed (white) because the diffraction peaks were indistinct and could not be indexed automatically—an exemplary Laue pattern from an unindexed pixel is shown in the figure. Though it could not be indexed automatically, by comparison with sharper patterns in Figure 7, this indistinct pattern is clearly from the twin. From Figure 6, the inclination angle between the T2 twin and the sample surface was about 40 deg, close to the calculated value (~38 deg) based on the parent grain orientation. Near the surface, the thickness of the twin along the tensile direction (horizontal) was ranging from about 7 to 8 μm, but further from the surface, the twin was not quite as thick. The surface topography revealed in this figure is consistent with the SEM observation in that the surface to the right of the twin was slightly higher than the surface to the left of the twin.

Every Laue pattern from this scan was manually examined. In Figure 7, pixels are colored based on the appearance of their Laue patterns. In the matrix, the yellow region and the red region display streaked Laue peaks but in different directions. Two typical Laue patterns (*a* and *b*) from these two regions are shown in Figure 7. It can be inferred that the yellow region and the red region contain different types of GNDs. In the

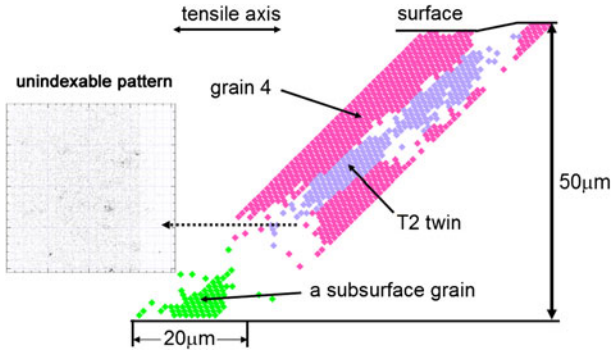

Fig. 6—A Laue microdiffraction line scan revealing the subsurface structure of the T2 twin in Grain 4. A subsurface grain was also identified. Laue patterns in the white regions cannot be indexed automatically.

twin, streaked Laue peaks were also observed in the dark green region and the light green region along different directions (patterns *d* and *f*). The light gray regions show peaks that are often broadened, but do not contain obvious streaks (*e.g.*, patterns *c* and *g*), implying much less GND content. The dark gray regions display complex shaped Laue peaks with strong curvature instead of straight streaks (*e.g.*, pattern *e*).

Peak streak analysis was performed based upon the assumption of edge dislocations to identify the GNDs in the yellow, red, dark green, and light green regions where straight streaked peaks were present. Initially, streak directions for only the 24 regular slip systems for Ti[1] were computed (3 basal slip, 3 prismatic slip, 6 pyramidal $\langle a \rangle$ slip, and 12 pyramidal $\langle c + a \rangle$ slip). This analysis showed that the streaks in the yellow region in the matrix are consistent with $(0\bar{1}11)[\bar{1}2\bar{1}3]$ edge GNDs (same slip system as the surface slip traces, with a global Schmid factor of 0.447), and the streaks in the red region are consistent with $(1\bar{1}01)[\bar{1}2\bar{1}3]$ edge GNDs (Schmid factor = 0.377). None of the 24 regular slip systems

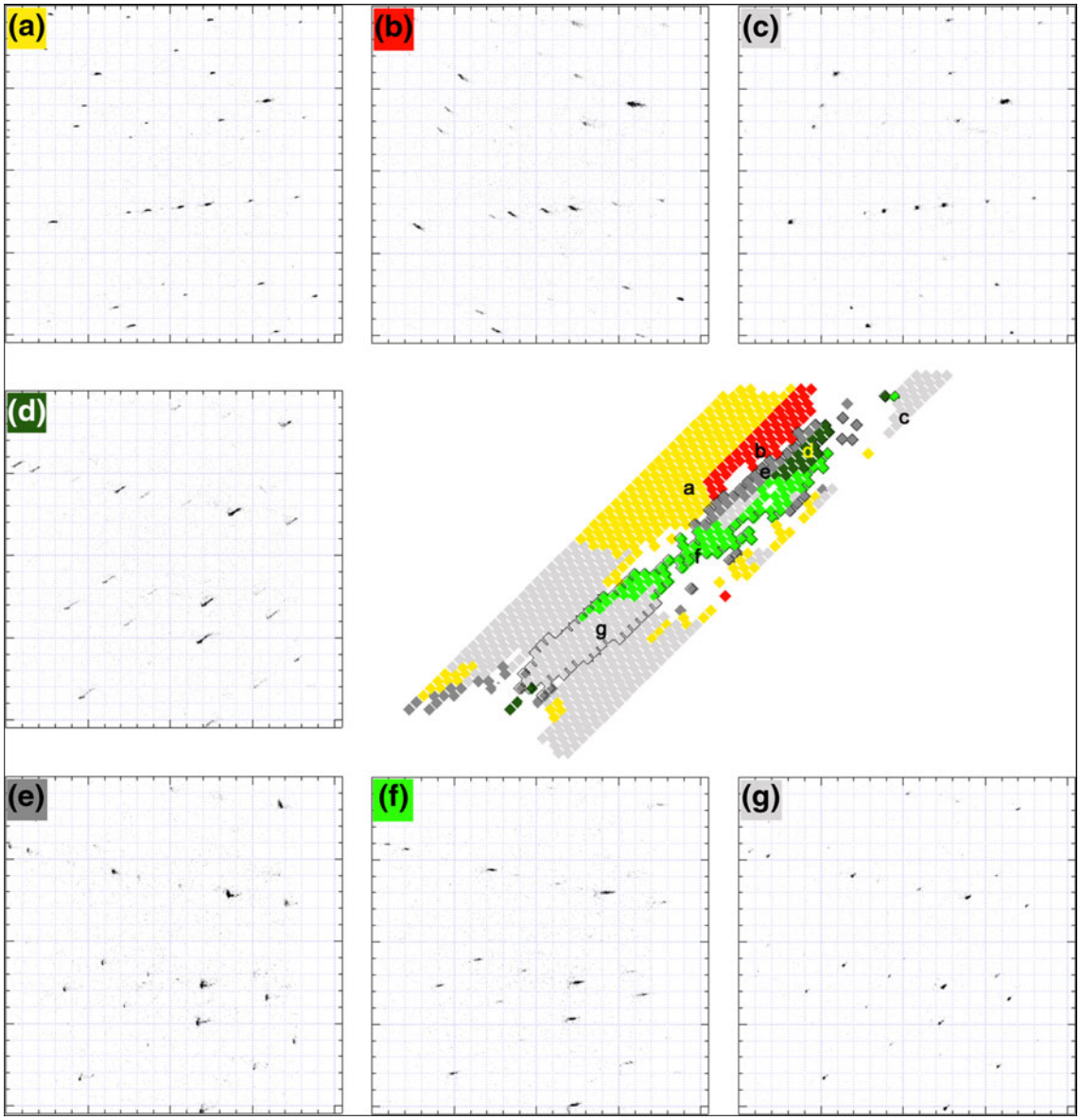

Fig. 7—Subdivision of Grain 4 (matrix) and the T2 twin based on the appearance of Laue patterns. The twin is between the black boundaries. Laue patterns of selected pixels (*a* through *g*) are shown. In the matrix, the yellow region and the red region have streaked peaks (*e.g.*, patterns *a* and *b*). In the twin, the dark green region and the light green region also show streaked peaks (*e.g.*, patterns *d* and *f*). GNDs in these colored regions are analyzed in Fig. 8. The light gray regions show no apparent streaked peaks (*e.g.*, pattern *c* from the matrix and pattern *g* from the twin). The dark gray regions have complex shaped diffraction peaks (*e.g.*, pattern *e*).

could account for the peak streak in the twin, and so streak directions for more slip systems were computed. From this additional analysis, $(\bar{1}\bar{1}21)_T[1\bar{2}1\bar{3}]_T$ edge GNDs (Schmid factor = 0.330) were found for the dark green region, and $(\bar{1}010)_T[1\bar{2}1\bar{3}]_T$ edge GNDs (Schmid factor = 0.457) for the light green region. Simulated patterns (using the method described in[45]) based on these edge GNDs matches patterns *a*, *b*, *d*, and *f* very closely, as shown in Figure 8. These four GND slip systems are visualized in the matrix unit cell ((φ_1, Φ, φ_2) = (175 deg, 66 deg, 2 deg)) and the twin unit cell ((φ_1, Φ, φ_2) = (22 deg, 143 deg, 75 deg)). The $(\bar{1}\bar{1}21)_T[1\bar{2}1\bar{3}]_T$ dislocations have been previously observed by Vaidya and Mahajan using TEM in the vicinity of T2 twins in Co.[17]

IV. DISCUSSION

A. *Transmission of $\langle c + a \rangle$ Dislocations Across T2 Twin Boundary*

Combining the results from surface slip trace and peak streak analysis, all of the identified dislocations in Grain 4 and the T2 twin had the same $\langle c + a \rangle$ Burgers vector—$\frac{1}{3}[\bar{1}2\bar{1}3]$ that is parallel to the twin plane $(\bar{1}\bar{1}21)$. These dislocations were identified on six different planes, as summarized in Figure 9(a). Near the left (dark green) TB, evidence for edge GNDs on $(0\bar{1}11), (1\bar{1}01), (\bar{1}\bar{1}21)$ (equivalent to $(\bar{1}\bar{1}21)_T$ because it is the twinning plane), and $(\bar{1}010)_T$ were identified. $(0\bar{1}11)[\bar{1}2\bar{1}3]$ was the primary active slip system in the matrix. It is likely that most of the slip activity in Grain 4 took place after the

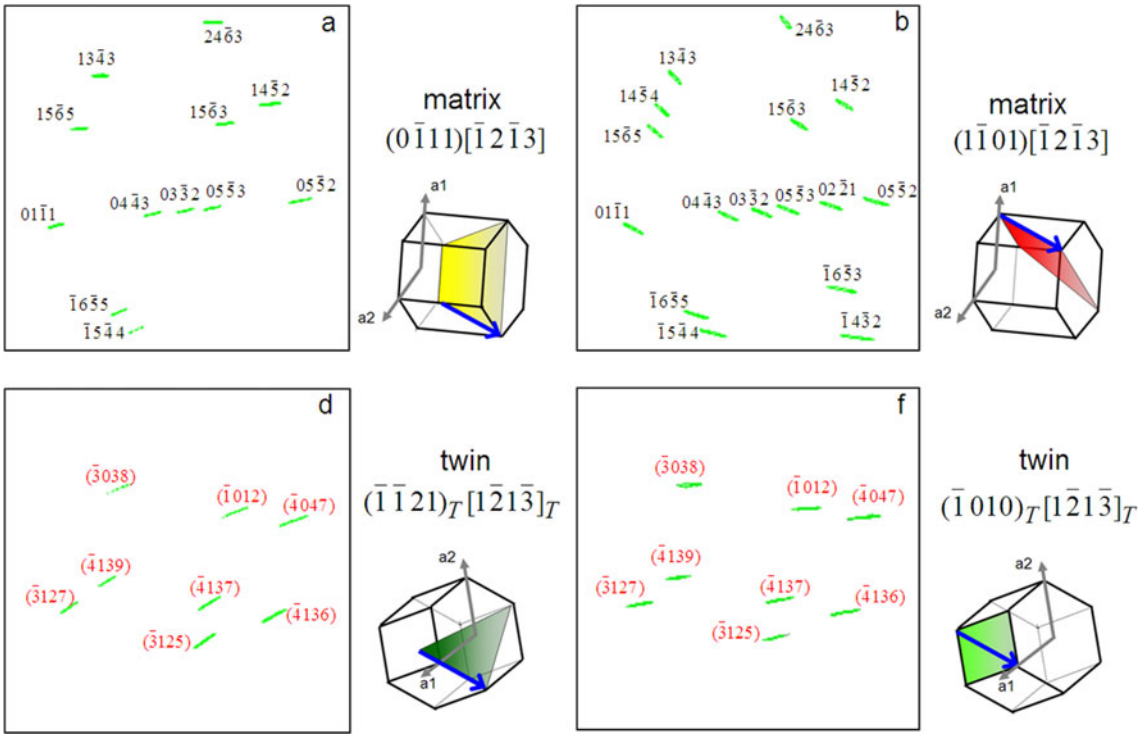

Fig. 8—Slip systems of GNDs in the yellow, red, dark green, and light green regions in Fig. 7 are identified as $(0\bar{1}11)[\bar{1}2\bar{1}3]$, $(1\bar{1}01)[\bar{1}2\bar{1}3]$, $(\bar{1}\bar{1}21)_T[1\bar{2}\bar{1}3]_T$ and $(\bar{1}010)_T[1\bar{2}\bar{1}3]_T$, respectively. The simulated Laue patterns based on edge GNDs on these four slip systems match the experimental patterns (*a*, *b*, *d*, and *f*) in Fig. 7. Peak indices are black for the matrix lattice and red for the twin lattice. These 4 activated slip systems are visualized in the unit cells of the matrix and the twin.

T2 twin formed across the grain. While the twin continued its thickwise growth, interaction between it and the concurrent matrix slip on its left side caused the roughness of the left TB. $(1\bar{1}01)[\bar{1}2\bar{1}3]$ and $(\bar{1}\bar{1}21)_T[1\bar{2}\bar{1}3]_T$ GNDs were likely the result of cross slip, as illustrated in Figure 9(b): a $(0\bar{1}11)[\bar{1}2\bar{1}3]$ dislocation loop expanded on the yellow plane until its leading screw component encountered the TB (dark green plane). Because it is parallel to the twin plane, this screw component could continue to glide on $(1\bar{1}01)$ and $(\bar{1}\bar{1}21)$, leaving edge components behind. These edge components probably had low mobility because their movement would result in a jog on the interface, which is energetically unfavorable. If $(0\bar{1}11)[\bar{1}2\bar{1}3]$ loops continued to nucleated on the yellow plane and cross slip their leading screw components to $(1\bar{1}01)$ and $(\bar{1}\bar{1}21)$, then edge $\langle c + a \rangle$ dislocations on those three planes would be accumulated at and near the interface. This mechanism can account for the $(0\bar{1}11)[\bar{1}2\bar{1}3]$, $(1\bar{1}01)[\bar{1}2\bar{1}3]$ and $(\bar{1}\bar{1}21)_T[1\bar{2}\bar{1}3]_T$ edge GNDs that were identified by peak streak analysis. The misalignment between $(0\bar{1}11)$ and $(\bar{1}010)_T$ is only about 5.3 deg, and so the uncommon prismatic $\langle c + a \rangle$ dislocations of $(\bar{1}010)_T[1\bar{2}\bar{1}3]_T$ in the light green region, which were present across the entire twin as shown in Figure 7, are probably a transmutation of the primary matrix dislocations $(0\bar{1}11)[\bar{1}2\bar{1}3]$ that are captured in the twin lattice during twin growth.[15] Near the right TB, slip traces of $(0\bar{1}11)[\bar{1}2\bar{1}3]$ within the matrix, and $(0\bar{1}11)_T[1\bar{2}\bar{1}3]_T$ and $(\bar{1}10\bar{1})_T[1\bar{2}\bar{1}3]_T$ within the twin were identified on the surface (Figure 4(c)). Activation of $(0\bar{1}11)_T[1\bar{2}\bar{1}3]_T$ and $(\bar{1}10\bar{1})_T[1\bar{2}\bar{1}3]_T$ was likely to arise from slip transmission, as indicated above before.

B. *Nucleation and Growth of T2 Twins*

In general, a few unique features were found for the observed T2 twins. Based on this, some discussion on their nucleation and growth mechanisms is offered here.

One observation is that all the T2 twins in Grains 1-5 seemed to nucleate from grain boundaries that were impinged by other T1 or T2 twins from the neighboring grain (T2 + T1 or T2 + T2). This mechanism also accounts for about 39 pct of the T1 twins that were identified in this specimen. For example, the two T1 twins in Grain 3 were apparently stimulated by T1 twins from adjacent grains (T1 + T1). According to a prior study, a critical condition for T1 + T1 to occur is that the operating twinning systems on the two sides of the grain boundary have a high $m' = \cos\kappa \cdot \cos\psi$, where κ and ψ are the angles between their twinning Burgers vectors and their twinning plane normals.[56] m' (ranging from 0 to 1) essentially measures the tendency for strain to transfer from one twinning system to the other across a grain boundary. Overall, high m' was found for most T2 + T1 or T2 + T2 examples. For example, between the pink T2 twin in Grain 1 and the green T1 twin in the upper neighboring grain (circled in Figure 2(b)), $m' = 0.77$; between the T2 twin in Grain 3 and the blue T1 twin in the lower grain (Figure 1), $m' = 0.97$; between the T2 twins in Grain 4 and Grain 5, $m' = 0.92$. On the other hand, with the type of

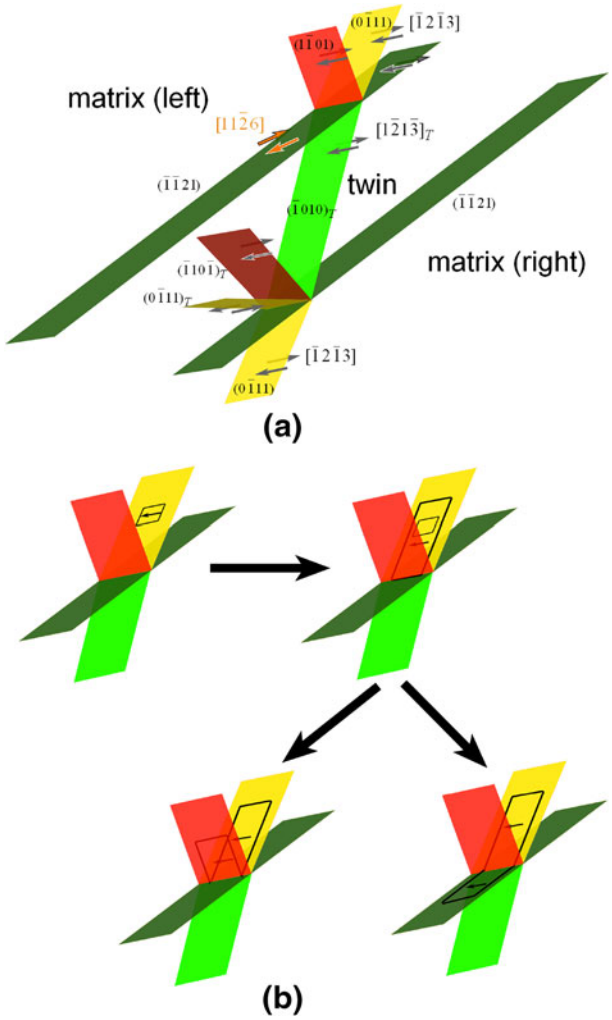

Fig. 9—(*a*) Summary of observed dislocation activities around the twin. All the identified dislocations had the same $\langle c + a \rangle$ Burgers vector: $\frac{1}{3}[\bar{1}2\bar{1}3]$ or $\frac{1}{3}[1\bar{2}1\bar{3}]_T$. This $\langle c + a \rangle$ Burgers vector was about 27.5 deg from the twinning direction $[11\bar{2}6]$. (*b*) Dislocation loop $(0\bar{1}11)[\bar{1}2\bar{1}3]$ expanded freely on the yellow plane until its leading screw component reached the TB. This screw component could cross slip from $(0\bar{1}11)$ to $(1\bar{1}01)$ and $(\bar{1}\bar{1}21)$, leaving edge components behind. These edge components, pinned at the TB, might later become GNDs that caused streaked peaks.

information we have, it is difficult to fully identify the underlying mechanisms (*e.g.*, stress concentration, pile-up of certain dislocations, etc.) that make certain grain boundaries become T2 twin nucleation sites. Crystal plasticity finite element modeling (CPFEM), TEM observation, and atomistic simulation may be necessary tools to further explore T2 twin nucleation mechanisms at different length scales.

After nucleation, the growth of a twin is usually accomplished by the glide of twinning dislocations on the TB. For T2 twinning, $\mathbf{b_{T2}} = \frac{1}{3(4\gamma^2+1)}\langle 11\bar{2}6\rangle = \frac{1}{3(4\times 1.59^2+1)}\langle 11\bar{2}6\rangle \approx \frac{1}{33}\langle 11\bar{2}6\rangle$.[22] Each growing step would require the spreading of this Burgers vector on 33 adjacent $\{\bar{1}\bar{1}21\}$ planes, which may be difficult. T2 twinning has an interesting feature in that its conjugate twinning plane K2 is (0001) and the conjugate shear direction $\eta 2$ is $[\bar{1}\bar{1}20]$, as shown in Figure 10. Bullough[57] first proposed an alternative twin growth model in which a simple shear on K2 in the direction $\eta 2$ is followed by a rotation about the normal of the plane of shear ($[1\bar{1}00]$ for the case of T2 twinning). Freise *et al.*[58] and Reed-Hill *et al.*[37] observed kinks near T2 TBs that corresponded to additional rotation around the $[1\bar{1}00]$ axis in graphite and Zr, which they concluded as evidence favoring Bullough's model. Observation of the intermediate orientation on the TB of the pink T2 twin in Grain 1 as well as the large orientation gradients in the T2 twin in Grain 4 in the current study seem also consistent with Bullough's model. It should be stated that Bullough's model is still controversial. Further study of the TB structure using high-resolution TEM and/or atomistic simulation is necessary to assess this model.

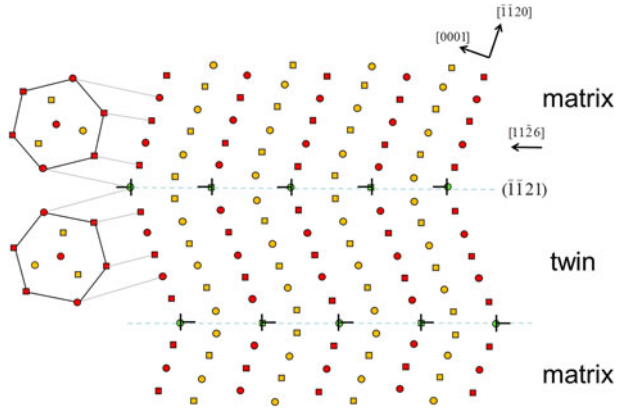

Fig. 10—$(1\bar{1}00)$ projection of the relaxed atom structure of $(\bar{1}\bar{1}21)$ TBs. $\eta 1$ is along $[11\bar{2}6]$ and $\eta 2$ is along $[\bar{1}\bar{1}20]$. Stacking sequence on the basal plane is also shown for both the matrix and the twin.

Combing the above discussion, it is proposed that T2 twin nucleation at a grain boundary is often triggered or facilitated by twinning in the adjacent grain. Growth of a T2 twin may be achieved by twinning dislocation gliding on K1 plane (conventional model) or by localized slip on K2 plane (a more controversial model).

V. CONCLUSIONS

T2 twins in a low strained commercial purity Ti sample were investigated. However, in a small number compared with T1 twins, T2 twins display some unique morphological features, such as irregular TBs, large orientation variation, and visible damage nucleation. Pyramidal $\langle c + a \rangle$ dislocations, with their Burgers vector parallel to the twinning plane, can cross slip their screw component into the twin and leave edge component piled up near the TB. Growth of the twin can engulf some pyramidal $\langle c + a \rangle$ dislocations and transmute them onto a prismatic plane in the twin lattice. Nucleation of T2 twins at grain boundaries may involve activation of twins from the same place in the neighboring grain, perhaps to accommodate strain transfer. Observation of intermediate orientation near some TBs might support a unique (also controversial) growth mechanism for T2 twins that involves localized slip on the K2 plane.

ACKNOWLEDGMENTS

This research was supported by a grant from Materials World Network from NSF (DMR-0710570) and DFG (EI 681/2-1). Use of the Advanced Photon Source was supported by the U.S. Department of Energy, Office of Science, Office of Basic Energy Sciences, under Contract No. DE-AC02-06CH11357. RIB was supported by the U.S. Department of Energy, Office of Basic Energy Sciences, Division of Materials Sciences and Engineering. Discussions with Jian Wang at Los Alamos National Laboratory have contributed to our understanding, and facilitated development of ideas presented in the current article.

REFERENCES

1. M.H. Yoo: *Metall. Trans. A*, 1981, vol. 12A, pp. 409–18.
2. M.R. Barnett: *Mater. Sci. Eng., A*, 2007, vol. 464, pp. 1–7.
3. A.M. Grade, E. Aigeltinger, and R.E. Reed-Hill: *Metall. Trans.*, 1973, vol. 4, pp. 2461–68.
4. L. Remy: *Metall. Trans. A*, 1981, vol. 12A, pp. 387–408.
5. A.A. Salem, S.R. Kalidindi, and R.D. Doherty: *Acta Mater.*, 2003, vol. 51, pp. 4225–37.
6. G.C. Kaschner, C.N. Tomé, I.J. Beyerlein, S.C. Vogel, D.W. Brown, and R.J. McCabe: *Acta Mater.*, 2006, vol. 54, pp. 2887–96.
7. C.N. Tomé, P.J. Maudlin, R.A. Lebensohn, and G.C. Kaschner: *Acta Mater.*, 2001, vol. 49, pp. 3085–96.
8. A.A. Salem, S.R. Kalidindi, and S.L. Semiatin: *Acta Mater.*, 2005, vol. 53, pp. 3495–502.
9. A.W. Sleeswyk and C.A. Verbraak: *Acta Metall.*, 1961, vol. 9, pp. 917–27.
10. S. Mahajan and G.Y. Chin: *Acta Metall.*, 1973, vol. 21, pp. 173–79.
11. B.A. Bilby and A.G. Crocker: *Proc. Phys. Soc. A*, 1965, vol. 288, pp. 240–55.
12. I. Saxl: *Czech. J. Phy.*, 1967, vol. 17, pp. 586–94.
13. Z.S. Bsinski, M.S. Szczerba, M. Niewczas, J.D. Embury, and S.J. Basinski: *Revue de Metall.*, 1997, vol. 94, pp. 1037–43.
14. H. El Kadiri and A.L. Opedal: *J. Mech. Phys. Solids*, 2010, vol. 58, pp. 613–24.
15. M. Niewczas: *Acta Mater.*, 2010, vol. 58, pp. 5848–57.
16. P.L. Pratt: *Acta Metall.*, 1953, vol. 1, pp. 692–99.
17. S. Vaidya and S. Mahajan: *Acta Metall.*, 1980, vol. 28, pp. 1123–31.
18. A.W. Sleeswyk: *Acta Metall.*, 1962, vol. 10, pp. 803–12.
19. B.A. Simkin, B.C. Ng, M.A. Crimp, and T.R. Bieler: *Intermetallics*, 2007, vol. 15, pp. 55–60.
20. T.R. Bieler, P. Eisenlohr, F. Roters, D. Kumar, D.E. Mason, M.A. Crimp, and D. Raabe: *Int. J. Plast.*, 2009, vol. 25, pp. 1655–83.
21. C.N. Tomé, I.J. Beyerlein, J. Wang, and R.J. McCabe: *JOM*, 2011, vol. 63, pp. 19–23.
22. J.W. Christian and S. Mahajan: *Prog. Mater. Sci.*, 1995, vol. 39, pp. 1–157.
23. M.H. Yoo, J.R. Morris, K.M. Ho, and S.R. Agnew: *Metall. Mater. Trans. A*, 2002, vol. 33A, pp. 813–22.
24. S.G. Song and G.T. Gray, III: *Acta Metall. Mater.*, 1995, vol. 43, pp. 2339–50.
25. J.F. Bingert, T.A. Mason, G.C. Kaschner, P.J. Maudlin, and G.T. Gray, III: *Metall. Mater. Trans. A*, 2002, vol. 33A, pp. 955–63.
26. N. Stanford, U. Carlson, and M.R. Barnett: *Metall. Mater. Trans. A*, 2008, vol. 39A, pp. 934–44.
27. D. Bhattacharyya, E.K. Cerreta, R.J. McCabe, M. Niewczas, G.T. Gray III, A. Misra, and C.N. Tome: *Acta Mater.*, 2009, vol. 57, pp. 305–15.
28. I.J. Beyerlein, L. Capolungo, P.E. Marshall, R.J. McCabe, and C.N. Tomé: *Phil. Mag.*, 2010, vol. 90, pp. 2161–90.
29. N. Bozzolo, L.S. Chan, and A.D. Rollett: *J. Appl. Crystallogr.*, 2010, vol. 43, pp. 596–602.
30. N. Thompson and D.J. Millard: *Phil. Mag.*, 1952, vol. 43, pp. 422–40.
31. S. Mendelson: *J. Appl. Phys.*, 1970, vol. 41, pp. 1893–1910.
32. A. Serra and D.J. Bacon: *Phil. Mag.*, 1996, vol. 73, pp. 333–43.
33. J. Wang, J.P. Hirth, and C.N. Tomé: *Acta Mater.*, 2009, vol. 57, pp. 5521–30.
34. B. Li and E. Ma: *Phys. Rev. Lett.*, 2009, vol. 103, p. 035503.
35. J. Wang, I.J. Beyerlein, and C.N. Tomé: *Scripta Mater.*, 2010, vol. 63, pp. 741–46.
36. L. Wang, Y. Yang, P. Eisenlohr, T.R. Bieler, M.A. Crimp, and D.E. Mason: *Metall. Mater. Trans. A*, 2010, vol. 41A, pp. 421–30.
37. R.E. Reed-Hill, W.H. Hartt, and W.A. Slippy WA: *Trans. AIME*, 1968, vol. 242, pp. 2211–15.
38. L. Capolungo, P.E. Marshall, R.J. McCabe, I.J. Beyerlein, and C.N. Tomé: *Acta Mater.*, 2009, vol. 57, pp. 6047–56.
39. N. Stanford: *Phil. Mag. Lett.*, 2008, vol. 88, pp. 379–86.
40. S.K. Mishra, P. Pant, K. Narasimhan, A.D. Rollett, and I. Samajdar: *Scripta Mater.*, 2009, vol. 61, pp. 273–76.
41. M. Calcagnotto, D. Ponge, E. Demir, and D. Raabe: *Mater. Sci. Eng., A*, 2010, vol. 527, pp. 2738–46.
42. B.C. Larson, W. Yang, G.E. Ice, J.D. Budai, and J.Z. Tischler: *Nature*, 2002, vol. 415, pp. 887–90.
43. W. Liu, G.E. Ice, B.C. Larson, W. Yang, J.Z. Tischler, and J.D. Budai: *Metall. Mater. Trans. A*, 2004, vol. 35A, pp. 1963–67.
44. W. Liu, G.E. Ice, B.C. Larsen, W. Yang, and J.Z. Tischler: *Ultramicroscopy*, 2005, vol. 103, pp. 199–204.
45. G.E. Ice and R.I. Barabash: *White Beam Microdiffraction and Dislocations Gradients. Dislocations in Solids*, Chap. 79, 2007, vol. 13, pp. 500–601.
46. R.I. Barabash, G.E. Ice, B.C. Larson, G.M. Pharr, K.-S. Chung, and W. Yang: *Appl. Phys. Lett.*, 2001, vol. 79, pp. 749–51.
47. R.I. Barabash, G.E. Ice, and F.J. Walker: *J. Appl. Phys.*, 2003, vol. 93, pp. 1457–64.
48. B. Wagenknecht, D. Libiran, S. Poon, and K. Sztykiel: In-*situ Four-Point Bending Apparatus for Scanning Electron Microscopes*, Senior Design Project, Mechanical Engineering, Michigan State University, April 2008.
49. L. Wang, R.I. Barabash, Y. Yang, T.R. Bieler, M.A. Crimp P. Eisenlohr, W. Liu, and G.E. Ice: *Metall. Mater. Trans. A*, 2011, vol. 42A, pp. 626–35.
50. J.F. Nye: *Acta Metall.*, 1953, vol. 1, pp. 153–62.
51. A. Arsenlis and D.M. Parks: *Acta Mater.*, 1999, vol. 47, pp. 1597–1611.
52. W. Pantleon: *Scripta Mater.*, 2008, vol. 58, pp. 994–97.
53. R.I. Barabash, G.E. Ice, W. Liu, and O.M. Barabash: *Micron*, 2009, vol. 40, pp. 28–36.
54. R. Maass, S. Van Petegem, H. Van Swygenhoven, P.M. Derlet, C.A. Volkert, and D. Grolimund: *Phys. Rev. Lett.*, 2007, vol. 99, p. 145505.
55. R. Maass, S. Van Petegem, D.C. Ma, J. Zimmermann, D. Grolimund, F. Roters, H. Van Swygenhoven, and D. Raabe: *Acta Mater.*, 2009, vol. 57, pp. 5996–6005.
56. L. Wang, P. Eisenlohr, Y. Yang, T.R. Bieler, and M.A. Crimp: *Scripta Mater.*, 2010, vol. 63, pp. 827–30.
57. R. Bullough: *Proc. Phys. Soc. A*, 1957, vol. 24, pp. 568–77.
58. E.J. Freise and A. Kelly: *Proc. Phys. Soc. A*, 1961, vol. 264, pp. 269–76.